Publications of the Astronomical Society of Australia (2026), **43**, e009, 14 pages
doi:10.1017/pasa.2025.10140

CAMBRIDGE UNIVERSITY PRESS

Research Article

The Deeper, Wider, Faster programme's first DECam optical data release

James Freeburn[1,2], Jeff Cooke[1,2], Anais Möller[1,2], Jielai Zhang[1,2], Dougal Dobie[2,3], Brent Miszalski[4], Simon O'Toole[4], James Tocknell[4], Sam Huynh[4], Sara Webb[1,2], Igor Andreoni[5], Natasha Van Bemmel[1,2], Timothy Abbott[6], Rebecca Allen[1,2], Stephanie Bernard[7], Simon Goode[2,8], Sarah Hegarty[1], J. Chuck Horst[9], Cassidy Mihalenko[2,10] and Mark Suhr[1]

[1]Centre for Astrophysics and Supercomputing, Swinburne University of Technology, Hawthorn, VIC, Australia, [2]ARC Centre of Excellence for Gravitational Wave Discovery, Hawthorn, VIC, Australia, [3]Sydney Institute for Astronomy, School of Physics, University of Sydney, Sydney, NSW, Australia, [4]Australian Astronomical Optics, Faculty of Science and Engineering, Macquarie University, North Ryde, Australia, [5]Department of Physics and Astronomy, University of North Carolina at Chapel Hill, Chapel Hill, NC, USA, [6]NOIRLab/MSO/CTIO Casilla 603, La Serena, Chile, [7]School of Physics, University of Melbourne, Parkville, VIC, Australia, [8]School of Physics and Astronomy, Monash University, Melbourne, VIC, Australia, [9]Department of Astronomy, San Diego State University, San Diego, CA, USA and [10]School of Natural Sciences, University of Tasmania, Private Bag 37 Hobart, Tasmania, Australia

Abstract

The transient and variable optical sky is relatively poorly characterised on fast (<1 h) timescales. With the dark energy camera (DECam), the Deeper, Wider, Faster programme (DWF) probes a unique parameter space with its deep (median of $g \sim 22.2$ AB mag), minute-cadence imaging. In this work, we present DWF's first data release which comprises high cadence photometry extracted from ∼12 000 images and 166 h of telescope time. We present a novel data processing pipeline, `dwf-postpipe`, developed to identify sources and extract their light curves. The accuracy of the photometry is assessed by cross-matching to public catalogues. In addition, we injected a population of synthetic GRB afterglows into a subset of the DWF DECam imaging to compare the efficiency of our pipeline with a standard difference imaging approach. Both pipelines show performance and reliably recover injected transients with peak magnitudes $g < 22$ AB mag with an efficiency of $97.24^{+0.7}_{-1.0}$ percent for `dwf-postpipe` and $96.14^{+0.9}_{-1.1}$ percent for a difference imaging approach. However, we find that `dwf-postpipe` is less likely to recover transients appearing in galaxies that are brighter or comparable in brightness to the transient itself. To demonstrate the power of the data in this release, we conduct a search for uncatalogued variable stars in a single night of DWF DECam imaging and find ten pulsating variables, two eclipsing binaries and one ZZ ceti. We also conduct a search for variable phenomena in the Chandra Deep Field South, a Rubin deep drilling field, and identify two flares from likely UV ceti type stars.

Keywords: Techniques: photometric; catalogues; stars: flare; stars: variables: general; methods: observational

(Received 9 June 2025; revised 17 November 2025; accepted 8 December 2025)

1. Introduction

The fast transient sky, events lasting less than ∼1 h duration, is not well characterised at optical wavelengths. Radio and high energy facilities are readily capable of detecting short (millisecond-to-hour) duration transients such as fast radio bursts (FRBs; Lorimer et al. 2007), Gamma-ray bursts (GRBs; Klebesadel, Strong, & Olson 1973) and Fast X-ray transients (FXRTs; Quirola-Vásquez et al. 2022, 2023). In optical and infrared however, the size and readout times of charged-coupled devices (CCDs) and wide field format arrays place limits on sky coverage and cadence compared to radio and high energy facilities for faint fast transients.

Despite this, there is a variety of observed optical transients which evolve on sub-hour timescales. The synchrotron afterglows originating from the forward shocks of jets launched from collapsars (Galama et al. 1997), neutron star mergers (Villasenor et al. 2005; Hjorth et al. 2005) and tidal-disruption events (Andreoni et al. 2022) exhibit rapidly decaying optical emission. Furthermore, the optical emission associated with a reverse shock can provide even more luminous optical transients decaying by multiple magnitudes over minute timescales (e.g. Akerlof et al. 1999; Lamb & Kobayashi 2019; Oganesyan et al. 2023). Observations of the Luminous Fast Blue Optical transient (LFBOT) AT2022tsd revealed luminous, minute-timescale flares (Ho et al. 2023). This phenomenon is not easily explained with the current understanding of LFBOT progenitors. Supernova shock-breakouts (Nakar & Sari 2010), occurring on minutes to hours timescales, have a number of known examples (Schawinski et al. 2008; Garnavich et al. 2016; Bersten et al. 2018). Some of the most commonly observed minute timescale optical transients are stellar flares which arise from magnetic reconnection processes from main-sequence stars (Moffett 1974).

There are also a number of theorised fast transients, which to-date, have not been observed. These include primordial black

Corresponding author: James Freeburn; Email: jamesfreeburn54@gmail.com

Cite this article: Freeburn J, Cooke J, Möller A, Zhang J, Dobie D, Miszalski B, O'Toole S, Tocknell J, Huynh S, Webb S, Andreoni I, Van Bemmel N, Abbott T, Allen R, Bernard S, Goode S, Hegarty S, Horst JC, Mihalenko C and Suhr M. (2026) The Deeper, Wider, Faster programme's first DECam optical data release. *Publications of the Astronomical Society of Australia* **43**, e009, 1–14. https://doi.org/10.1017/pasa.2025.10140

© The Author(s), 2025. Published by Cambridge University Press on behalf of Astronomical Society of Australia. This is an Open Access article, distributed under the terms of the Creative Commons Attribution licence (https://creativecommons.org/licenses/by/4.0/), which permits unrestricted re-use, distribution and reproduction, provided the original article is properly cited.

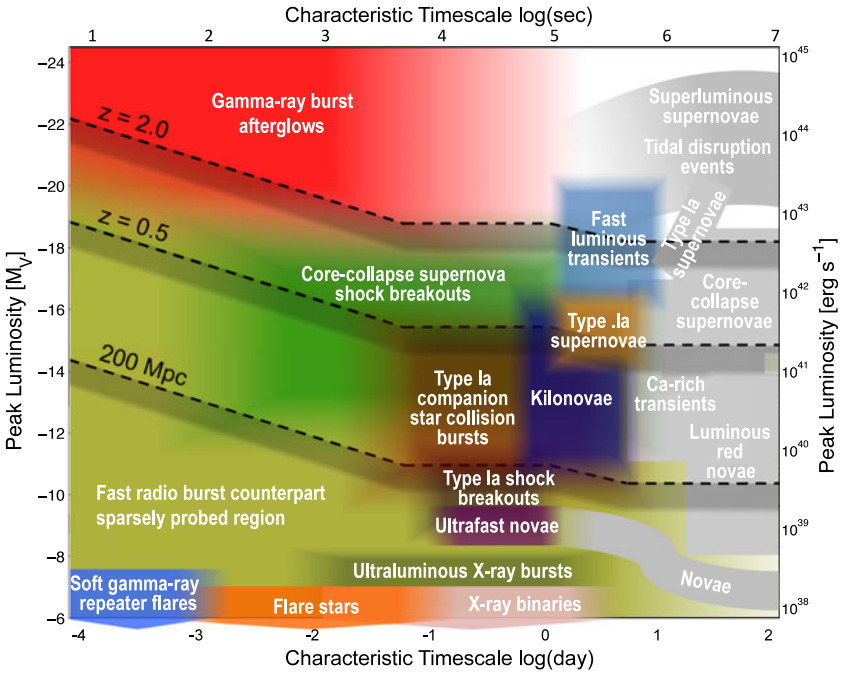


Figure 1. Approximate timescales and luminosities of known and theorised optical transients. The peak luminosities of Soft-gamma-ray repeater flares, flare stars and X-ray binaries extend lower than the axes shown on the plot for readability. Adapted from Cooke et al. in preparation.

hole micro-lensing (Rest et al. 2005) and possible optical counterparts to FRBs (Yi, Gao, & Zhang 2014; Yang, Zhang, & Wei 2019), blitzars (Falcke & Rezzolla 2014), synchrotron masers (Long & Pe'er 2018; Metzger, Margalit, & Sironi 2019) and white dwarf accretion-induced collapse (Margalit, Berger, & Metzger 2019).

There are a small number of surveys that have probed the fast transient sky in optical wavelengths at shallower depths. Evryscope (Law et al. 2015) is a dedicated fast transient survey, which possesses a 18 400 square degree field of view and a two minute cadence, and has detected a vast population of stellar flares (Howard et al. 2018, 2019). The Transiting Exoplanet Survey Satellite (TESS; Ricker et al. 2015) was designed primarily to detect transiting exoplanets from nearby, bright stars. However, in recent years, the TESS data has been appropriated for both targeted (e.g. Levan et al. 2024; Roxburgh et al. 2024; Jayaraman et al. 2024; Perley et al. 2025) and untargeted approaches to the identification of extragalactic fast transients (Roxburgh et al. 2025).

Evryscope and TESS have depths of ∼14 and 17 AB mag respectively. Only a small percentage of cosmological transients rise above these limits. Deeper surveys reach further into fast transient population luminosity distributions and probe larger cosmological volumes, allowing for more frequent transient detection. Traditional synoptic surveys such as the Zwicky Transient Facility (ZTF; Bellm et al. 2019), The Dark Energy Survey (DES; Dark Energy Survey Collaboration et al. 2016), Pan-STARRS1 (Kaiser et al. 2002) and the upcoming Vera C. Rubin Observatory's Legacy Survey of Space and Time (Rubin; Ivezić et al. 2019) have depths of ∼20.5, 23, 24, and 24.5 AB mag, respectively. However, their main surveys typically have cadences in excess of one day, although some some have conducted specialised, high-cadence experiments (e.g. Berger et al. 2013; Klein, Bellm, & Davenport 2019; Kupfer et al. 2021; Ho et al. 2024).

The Deeper, Wider, Faster programme (DWF; Andreoni & Cooke 2019) provides a dedicated deep survey for identifying fast optical transients on minute timescales to $m \sim 23$. Moreover, it is a transient survey which comprises simultaneous observations in radio, millimetre, optical, ultra-violet, X-ray, gamma-ray, and high-energy particles. Using the dark energy camera (DECam; Flaugher et al. 2015), mounted on the Victor M. Blanco 4m telescope, DWF probes a new parameter space in the search for fast optical transients with its depth, minute cadence and sky coverage. Subaru Hypter Suprime-Cam (Miyazaki et al. 2002) and KMTNet (Kim et al. 2016) have also been used for high cadence optical imaging during DWF runs but these data are not included in this data release.

In this paper, we describe the Deeper, Wider, Faster programme's first data release of the minute-cadence optical data obtained with DECam. In Section 2, we describe the observing strategy utilised with DWF, its uniqueness compared to other surveys and an overview of the DWF observing runs included in this data release. Section 3 describes the data processing pipeline, `dwf-postpipe`, which is used to produce the data products for this release, and we assess the data quality of the data products in Section 4. We identify a sample of uncatalogued variable stars using a single night of DWF DECam data and search the Chandra Deep Field South (CDFS), a Rubin deep-drilling field, for variable phenomena and identify two flare stars in Section 5. Section 6 discusses classification of the identified variables, potential applications of this dataset, and future facilities that will complement it.

2. Data

2.1. The minute-timescale optical sky

Transients with characteristic timescales of $\gtrsim 10^1$ d, which includes most classes of supernova (see Figure 1), are readily detected by traditional optical surveys, which typically revisit the

https://doi.org/10.1017/pasa.2025.10140 Published online by Cambridge University Press

same fields on daily to weekly cadences (Perley et al. 2020). In contrast, the minute-timescale sky is dominated by frequent Galactic events, such as flare stars (Moffett 1974; Haisch, Strong, & Rodono 1991), while extragalactic phenomena such as Gamma-ray burst afterglows (e.g. Ho et al. 2022; Freeburn et al. 2024) and theorised counterparts to fast radio bursts are far rarer (e.g. Price et al. 2018; Tingay & Yang 2019; Núñez et al. 2021; Hanmer et al. 2025). DWF probes the deep, minute-timescale optical sky in an effort to identify these rare classes.

DECam has been the dominant wide-field imager used in most DWF coordinated observing runs to detect minute-timescale optical transients and identify counterparts to multi-wavelength transients. Our team reduce and analyse the data in real-time with the `Mary` pipeline (Andreoni et al. 2017), aided by a convolutional neural network (Goode et al. 2022) and data visualisation tools (e.g. Meade et al. 2017, Hegarty, in preparation) to trigger rapid response target-of-opportunity observations.

To-date, the DECam dataset of DWF has been used to study the population of extragalactic fast transients (Andreoni et al. 2020), stellar flares (Webb et al. 2021; Clarke et al. 2025) and orphan afterglows (Freeburn et al. 2024), among other things. There have also been multiple, novel classification methods developed for DWF DECam light curves for different purposes (Webb et al. 2020b; Strausbaugh et al. 2022; Freeburn et al. 2024).

2.2. Observations included in this data release

For this data release, we include observations taken via the main observing strategy of DWF which involves taking continuous 20 s g-band exposures for periods ranging from ∼0.5–3 h per field. With DECam's ∼30 s overhead between exposures, this corresponds to a cadence of ∼50 s. On a given night, 2–5 fields are targeted and the observations are repeated for 6 consecutive nights during each observing run. As a result, each run produces 6 sets of nightly high cadence data for each field, separated by ∼21–23.5 h. For the remainder of this work, we refer to a given set of high-cadence observations for a specific field and night by 'field-night.'

To-date, there have been 14 DWF coordinated operational runs, denoted O1 through O14, from December 2015 to January 2025 and two Pilot runs in January and February 2015. During observing runs DWF O4, O8 and O11, the fast-cadenced optical observations were performed with Subaru Hyper Suprime-Cam and KMTNet, respectively. As this work reports specifically on the DWF DECam data, we exclude these runs. DWF O9 used an alternate strategy with dithered exposures and a larger number of fields tailored to detect kilonovae and had fewer exposures in each field per night which served as a pilot run for the Kilonova and Transients Programme (KNTraP; Van Bemmel et al. 2025). In addition, the two DWF pilot runs employed a dithering strategy, that is not compatible with the photometric pipeline in this data release. Finally, in DWF O13 and O14, three fields in the Large Magellanic Cloud were targeted. Due to the high density of sources, these fields are confusion limited by our processing and are therefore not included in this data release. As a result, we use only data from the remaining nine DWF runs. Occasionally, time was taken out of the main observing strategy for rapid target-of-opportunity observations of multi-wavelength transients (e.g. Freeburn et al. 2025a). These observations depart from the primary observing strategy of DWF and include longer exposure times, dithering and multiple filters. We therefore do not include these observations in this data release. Full details of DWF programme including all multi-wavelength facilities and operational runs will be described in Cooke et. al (in preparation).

Table 1. Fields and night coverage for this data release.

Field	Coordinates	Gal. latitude (°)	Runs	Nights
FRB010724	01:18:06 −75:12:19	−41.80	Dec 2015 (O1)	5
3hr	03:00:00 −55:25:00	−53.43	Dec 2015 (O1)	5
CDFS	03:30:24 −28:06:00	−54.93	Dec 2015 (O1), Dec 2019 (O7), Sep 2021 (O10), Sep 2022 (O12)	9
4hr	04:10:00 −55:00:00	−44.76	Dec 2015 (O1), Jan 2025 (O14)	11
Prime	05:55:07 −61:21:00	−30.26	Feb 2017 (O3)	5
FRB 131104	06:44:00 −51:16:00	−21.95	Feb 2017 (O3)	4
8hr	08:16:00 −78:45:00	−22.62	Jun 2018 (O5)	3
Dusty 10	10:12:00 −80:50:00	−19.96	Jun 2018 (O5)	2
Antlia	10:30:00 −35:20:00	19.17	Feb 2017 (O3), Jun 2018 (O5) Jan 2024 (O13)	11
Dusty 12	11:46:00 −84:33:00	−21.89	Jul 2016 (O2)	1
14hr	14:34:00 −78:06:00	−16.30	Jul 2016 (O2)	3
NGC 6101	16:26:00 −73:00:00	−16.37	Jul 2016 (O2), Aug 2016 (O2), Jun 2019 (O6)	12
NGC 6744	19:09:46 −63:51:27	−26.15	Jul 2016 (O2), Aug 2016 (O2), Jun 2019 (O6), Sep 2021 (O10), Sep 2022 (O12)	22
Field 3	21:00:00 −42:48:00	−49.41	Jun 2019 (O6)	2
NSF2	21:28:00 −66:48:00	−39.82	Jul 2016 (O2)	2
FRB190711	21:57:41 −80:21:29	−33.90	Sep 2021 (O10), Sep 2022 (O12)	11
FRB 171019	22:17:31 −08:39:32	−49.24	Dec 2019 (O7),	2
HDFS	22:33:26 −60:38:09	−49.22	Sep 2021 (O10)	2
Total				112

The remaining DECam observations are summarised in Table 1, comprising ∼ 12 000 images and 166 h of observing time over 112 field-nights. The median limiting magnitude and full width at half maximum (FWHM) value for each exposure across these field-nights is $g \sim 22.2$ and 1.35″ respectively. DWF is scheduled for 6 consecutive nights during dark time, with O2 being conducted across 13 nights. Consequently, 80% of DECam observing time is conducted with the moon below the horizon. The remaining 20% has a range of lunar illumination fractions. We remove nights where the median $> 5\sigma$ limiting magnitude is <21 AB mag. The resulting distributions are shown in Figure 2. Dark time observations have a comparatively deeper median limiting magnitude of $g = 22.3$ (5σ) than grey time, $g = 21.5$ (5σ). The median seeing value of 1.35″ remains consistent between bright

https://doi.org/10.1017/pasa.2025.10140 Published online by Cambridge University Press

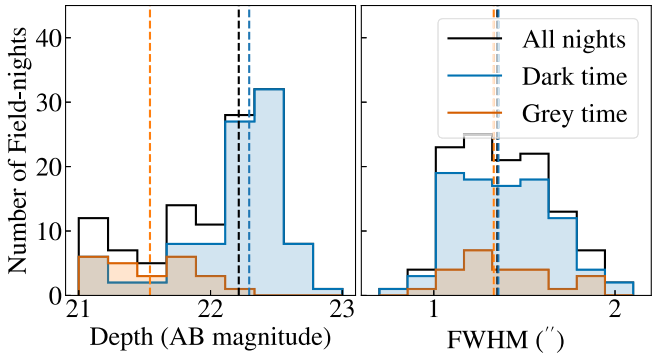


Figure 2. Histograms of the median *g*-band limiting magnitudes (left) and median seeing FWHM (right) for the field-nights included in this data release. The *g*-band depth and seeing FWHM are affected by the need for DECam observations to occur up to relatively high airmass (∼1.3–2.0) in order to enable simultaneous observations of each field by telescopes in Chile, Australia and other parts of the world. Dark time is defined as field-night observations that begin and end with a moon below the horizon and grey time is defined as those that begin or end with a moon altitude $> 0°$. The median values for each distribution are indicated by the vertical dashed lines.

and dark time observations. Given that 80% of DWF DECam observations were conducted during dark time, we obtain an overall median 5σ limiting magnitude of $g = 22.2$.

DWF is mainly designed to detect extragalactic fast transients and the fields are selected based on a number of criteria. The DECam observations probe a large cosmological volume and, as such, extragalactic transients can occur in any random pointing. However, fields are selected at high Galactic latitude, when possible, to minimise Galactic extinction for the optical and some shorter-wavelength observations. As searching for counterparts to fast radio bursts (FRBs) has been a main aim of DWF since its inception in 2014, some DWF fields target the sky location of repeating FRBs in an effort to detect a repeat burst with simultaneous, multi-wavelength coverage, while searching the wide-fields for new FRBs. Other considerations include targeting known galaxy clusters and legacy fields where there is a large amount of multi-wavelength data and spectroscopic characterisation of galaxies, and fields with previous DWF observations for temporal monitoring and deep image templates. Finally, field choice is constrained to fields that are simultaneously observable from the locations of each major multi-wavelength facility (often in Chile and Australia) participating in a given DWF observing run and the scheduled nights. The sky locations of the fields are shown in Figure 3 along with the number of nights on which they were observed.

3. DWF-postpipe

The real-time data processing pipeline, `Mary`, with a difference-imaging approach, enables the rapid identification of transients for triggering during DWF runs. In this work, we design a custom pipeline, `dwf-postpipe`, to be used in post-run to generate an archival dataset. `dwf-postpipe` does not utilise difference imaging. A light curve is produced for every object in the field, regardless of whether there is an observed change in brightness. This aids in the discovery of variable stars as, with a difference imaging approach, their detectability would depend on their phase when the template image was taken. It also reduces the number of artefacts due to poor alignment and image quality matching between templates and science images. We distinguish the three pipelines used for processing DWF DECam data mentioned in this work: `Mary` the real-time data processing pipeline; `dwf-postpipe`, the post-run pipeline described below; and `photpipe` (Rest et al. 2005, 2014), which is a separate pipeline used for comparative analysis in Section 4.2.

We designed `dwf-postpipe` primarily to produce intra-night, minute-cadence light curves reflecting the DWF DECam observing strategy and main goal of identifying transients evolving on minute timescales. The pipeline begins with the calibrated images from The DECam Community Pipeline (Valdes, Gruendl, & DES Project 2014), which applies corrections to cross-talk, overscan, fringing in addition to flat-fielding, bias-correction and an astrometric solution. It also performs cosmic ray and saturation rejection and background subtraction. It is a robust pipeline which produces good quality images, suitable for photometry. `dwf-postpipe` comprises three steps: Source identification, image matching and photometry. Below, we explain each step in detail and show a graphical representation of the pipeline in Figure 4. The data products from `dwf-postpipe` have already been utilised for a search for GRB afterglows (Freeburn et al. 2024) and assessing simultaneous optical and radio variability of radio transients found with the Australia Square Kilometer Array Pathfinder (Dobie et al. 2023).

3.1. Source identification

`dwf-postpipe` is designed to generate complete light curves for each source detected throughout the night for a given DECam pointing. In this effort, we want to ensure transient sources that rise above or fall below the detection threshold throughout the night are identified and measured. This requires two components; a 'master catalogue' of all of the sources detected throughout the night, transient or not, and a method to perform forced photometry at the location of each of these sources for every image taken throughout the night.

We use `SExtractor` (Bertin & Arnouts 1996), a code that detects, deblends, measures, and classifies sources in astronomical imaging. For source identification, we use `SExtractor`'s built-in background modelling algorithm which estimates the image background by calculating values from a mesh grid and interpolating across the image using a cubic spline. For photometry, background values for each source are estimated by using `SExtractor`'s `LOCAL` method, which is based on a rectangular annulus with a width of 24 pixels. `SExtractor` does not include an in-built method for performing forced photometry directly from a catalogue. However, `SExtractor` includes the capability to run in 'double image' mode that identifies sources from a 'detection image' and then measures photometry, classification and deblending on a 'measurement image.' We use this method for this pipeline.

To minimise the contamination of electronic artefacts in the master catalogue, we initially conduct a three-image rolling median coaddition. With this method, sources appearing in a single image in the night are not included in the master catalogue and do not have an associated light curve. `SExtractor` generates catalogues for each of these stacked images. The catalogues are then compiled into a master catalogue by cross-matching sources within one arcsecond of each successive catalogue. If a source in a successive catalogue is not cross-matched, has $>5\sigma$ detection and a FWHM within 1σ of the median, point-source value, it is appended to the master catalogue. This is to ensure only genuine

https://doi.org/10.1017/pasa.2025.10140 Published online by Cambridge University Press

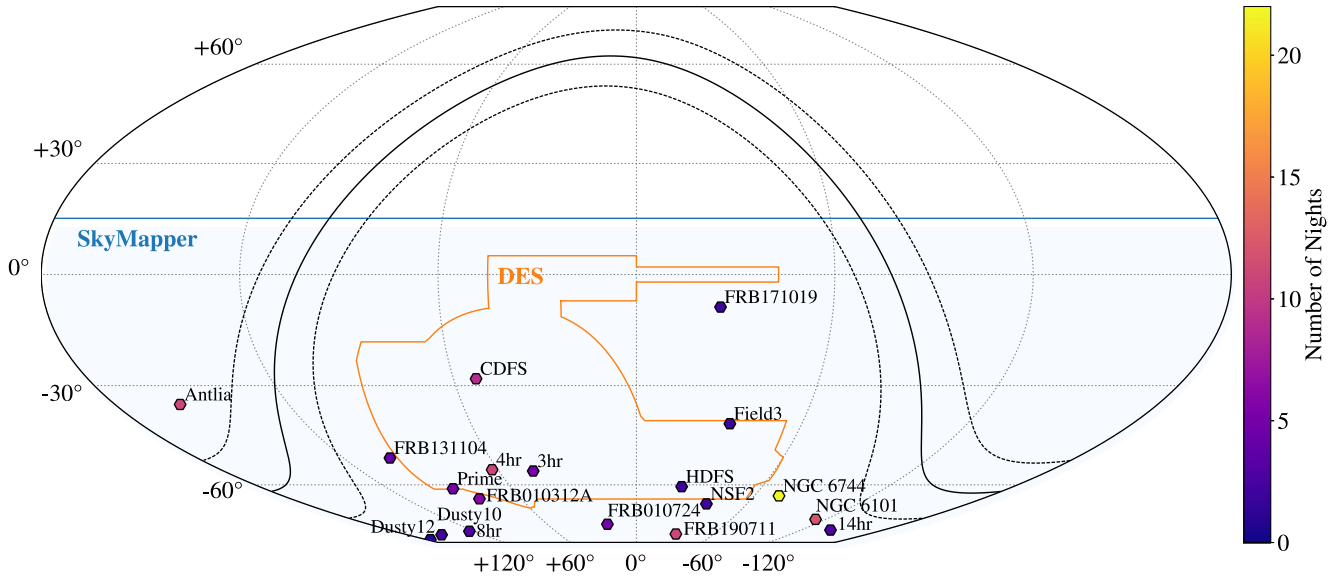


Figure 3. Sky locations of the DWF fields presented in this data release. A solid black line marks the Galactic plane and the dotted black lines denote ±10° from the plane. The number of nights each field has been observed is indicated by the colourbar on the right. The footprints of the SkyMapper Southern Survey DR4 (SMSS DR3; Onken et al. 2024) and DES (Dark Energy Survey Collaboration et al. 2016) are shown in blue and orange, respectively.

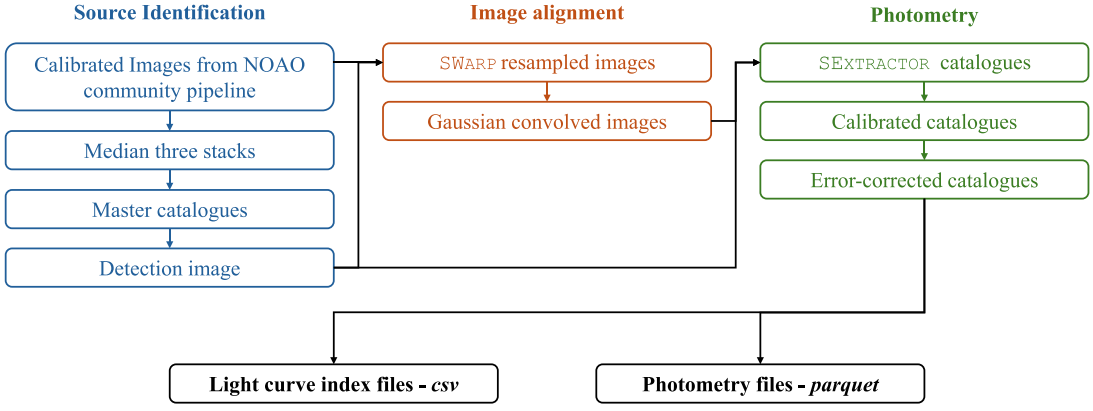


Figure 4. Schematic diagram of `dwf-postpipe` used in this data release. This methodology is applied to each of the 112 field-nights shown in Table 1.

transients are added to the master catalogue rather than electronic artefacts like cross-talk.

We select the detection image in a given night as the image with the highest point source seeing FWHM value to ensure the PSF is matched properly for each image in a field-night. This process is explained in more detail in Section 3.2. Sources that are in the master catalogue but do not appear in the detection image are artificially added to the detection image with a Moffat profile and a FWHM in accordance with the median, point-source value of the detection image. In dual-image mode, therefore, each source in the master catalogue is identified as a source in the detection image.

3.2. PSF matching

Once sources are added to the detection image, to ensure pixel-for-pixel alignment between images, we resample the each image for given field and night to the detection image using `Swarp` (Bertin 2010).

Variability in atmospheric seeing between images can result in flux from neighbouring sources contaminating photometry to varying degrees in different images. This induces time-correlated noise into the photometry of blended sources, which can easily be mistaken for astrophysical variability. To minimise this effect, we match each image's point spread function (PSF) to the detection image with a Gaussian convolution using `hotpants` (Becker 2015). Adopting the image with the highest FWHM value as the detection image ensures that the PSF of every other image of the night is degraded to match the detection image.

3.3. Photometry

Photometry is the third and final step of the pipeline. We use `SExtractor` in double-image mode with the resampled detection image to detect sources and the resampled, convolved images from the previous step for measurement. Because transient sources have been added to the detection image, this will be the complete set of

https://doi.org/10.1017/pasa.2025.10140 Published online by Cambridge University Press

sources for the night. *SkyMapper*'s (Onken et al. 2024) fourth data release (DR4) includes coverage of all the DWF fields included in this data release. We therefore use *SkyMapper* DR4 to calculate magnitude zeropoints for the instrumental photometry for each CCD for each exposure to ensure a uniform calibration.

`SExtractor` estimates the error of photometric measurement assuming Poisson statistics between uncorrelated pixels. With the Gaussian convolution induced by `hotpants`, neighbouring pixels become correlated, resulting in an underestimation of the flux error. To correct for this, we adopt an empirical approach to correct for the reduced effective number of statistically independent pixels. Due to the high cadence of the DWF data, successive images can be assumed to be similar in depth. Therefore, the median absolute differences in flux measurements of non-variable sources in successive exposures can be used to estimate the effective error associated the flux measurements. With this assumption, we can calculate estimate the true uncertainty by binning sources into magnitude bins and calculating the median difference in magnitude between a given exposure and the next. This difference is then compared to the median error in each of these bins. The flux error is then multiplied by a factor to resolve the disparity between the median error and median magnitude difference in each bin. This calculation is described in detail in Appendix A.

3.4. Data products

The above steps result in each source having a complete light curve over the course of a given night. The light curves from each night are combined for each field by cross-matching those within a one arcsecond radius and labelling each with a object identifier consistent between nights. With this object identifier, candidates can be monitored over DWF's ∼10 yr dataset.

An 'Apache Parquet' file is produced containing each photometric measurement for each source in each exposure over the entire DWF dataset which is called `lightcurve`. In addition, there is a light curve index file, `mastercatalogue`, containing a row for each source appearing over the course of a single night. Each row represents a nightly light curve that can be queried from the photometric catalogue. The rows contain light curve metadata, such that interesting light curves or objects can be identified without opening the large, photometric parquet file. These files will be supplied in this release in addition to the reduced images from the DECam community pipeline. The schema for these catalogues are shown in Tables B1 and B2 in Appendix B.

In Table 2, we summarise the quantity of candidates observed in this data release. To quantify variability we use the Von-Neumann statistic (von Neumann 1941),

$$\eta = \frac{\sum_{i=1}^{N-1} (m_{i+1} - m_i)^2/(N-1)}{\sum_{i=1}^{N} (m_{i+1} - \bar{m})^2/(N-1)} \quad (1)$$

which describes how much of the variance is explained by intrinsic variability versus random noise. m_i describes the series of measurements in the light curve and N is the total number of measurements in the light curve. This statistic has been shown to be reliable in identifying variable astrophysical phenomena (Sokolovsky et al. 2017). Of the 4 862 636 unique objects observed in all fields in this data release, we find that 92% of them do not exhibit significant variability ($\eta^{-1} < 1$). The remaining 8% include astrophysical transients and variables in addition to asteroids and electronic artefacts. We cross-match 6 927 of these objects with existing variable catalogues; *Gaia* DR3 (Gaia Collaboration et al. 2023), the ASAS-SN catalogue of variable stars (Jayasinghe et al. 2018) and the catalogue for RR Lyrae variable stars in DES Y6 (Stringer et al. 2021) which is shown in the known variables column in Table 2.

Table 2. Quantity of unique objects observed in this data release.

Field	Unique objects	Objects with $\eta^{-1} > 1$	Known variables
FRB010724	423 392	44 377	522
3hr	287 127	10 248	210
CDFS	269 714	6 776	705
4hr	370 886	20 749	238
Prime	279 211	9 752	315
FRB131104	175 979	5 987	361
8hr	136 299	6 173	316
Dusty10	168 121	3 248	372
Antlia	345 008	13 526	513
Dusty12	130 120	11 430	333
14hr	340 002	44 858	597
NGC 6101	499 261	83 556	832
NGC 6744	578 019	87 437	503
Field3	109 565	1 241	319
NSF2	658 64	6 818	245
FRB190711	544 302	44 043	230
FRB171019	517 68	892	111
HDFS	87 998	1 820	205
Total	4 862 636	402 931	6 927

3.5. AAO data central

The calibrated images from the DECam community pipeline (individual epochs) and `dwf-postpipe` light curves are hosted by the AAO Data Central science platform.[a,b] The AAO Data Central science platform provides a wide range of services to engage with DWF data products. The images and light curves are primarily accessible, respectively, via Data Central's Simple Image Access (SIA) and Table Access Protocol (TAP) services. These services enable both programmatic data access e.g. via Python or interactive data access e.g. via `topcat` (Taylor 2005). Individual objects of interest may also be visualised using Data Central's Single Object Viewer that facilitates interactive display of the images, light curves and other metadata in one place. Since these services are under active development, we refer to the latest documentation on the Data Central science platform for the latest information.

4. Data quality analysis

4.1. Photometric calibration

The DECam Local Volume Exploration Survey (DELVE; Drlica-Wagner et al. 2021) provides *g*-band, DECam imaging coverage of all DWF fields in this data release. With a 5σ limiting magnitude

[a] https://datacentral.org.au.
[b] https://doi.org/10.57891/gy62-bj96.

https://doi.org/10.1017/pasa.2025.10140 Published online by Cambridge University Press

Table 3. Data quality statistics of each DWF field included in this data release. Magnitude offsets of the median magnitude for each source in each DWF field are cross matched with DELVE photometry. We also show the density of sources in each field with the median number of sources found in each $9' \times 18'$ CCD.

Field	DELVE offset (mag)	Median depth (AB mag)	Median FWHM ($''$)	Median sources per CCD
FRB010724	-0.173 ± 0.027	21.5	1.5	2 830
3hr	-0.140 ± 0.022	21.5	1.5	1 039
CDFS	-0.157 ± 0.031	22.3	1.2	1 185
4hr	-0.151 ± 0.024	22.1	1.2	1 697
Prime	-0.159 ± 0.021	22.3	1.3	2 602
FRB 131104	-0.158 ± 0.015	22.4	1.4	1 445
8hr	-0.166 ± 0.013	21.8	1.5	1 525
Dusty 10	-0.162 ± 0.013	22.0	1.3	1 801
Antlia	-0.159 ± 0.013	22.4	1.1	2 917
Dusty 12	-0.168 ± 0.018	22.6	1.3	2 202
14hr	-0.160 ± 0.017	21.2	1.4	2 969
NGC 6101	-0.172 ± 0.013	22.3	1.6	3 520
NGC 6744	-0.139 ± 0.013	22.2	1.5	2 295
Field 3	-0.147 ± 0.022	22.4	1.7	1 305
NSF2	-0.137 ± 0.017	21.2	1.6	871
FRB190711	-0.158 ± 0.019	22.1	1.5	493
FRB171019	-0.146 ± 0.022	21.1	1.4	2 044
HDFS	-0.148 ± 0.017	22.0	1.4	1 311

of $g \sim 23.5$, it provides a useful direct comparison for the photometric pipeline presented in Section 3. We find that for each DWF field, there is a consistent offset from DELVE and no dependence with magnitude. We demonstrate this in Table 3. The ∼0.15 mag offset is due to our calibration with SMSS DR4, which has a systematic offset with DELVE. The systematic offset likely results from SMSS DR4's use of spectroscopic calibrator stars to calculate zero-points in contrast to DELVE's use of the ATLAS Refcat2 catalogue (Tonry et al. 2018).

4.2. Injection of synthetic transients

To assess `dwf-postpipe`'s performance, we compare the results of our pipeline to `photpipe` (Rest et al. 2005, 2014), a popular difference imaging pipeline for identifying transient sources.

For the difference image analysis using `photpipe`, templates were selected based on the availability of images taken during DWF operational runs with low seeing values. We coadd 5 NGC 6101 images and 10 CDFS images which have 5σ depths of $g =$ 23.2 and 23.6 AB mag respectively and FWHM values of $1.22''$ and $1.27''$ respectively.

We inject synthetic transients, hereafter called 'fakes', into the DWF data with `afterglowpy` (Ryan et al. 2020) using the procedure described in Freeburn et al. (2024). These events are well suited to test our pipeline due to their fast evolution (i.e. evolution in a single field-night observation). The fakes are injected directly into each image with a Moffat profile matched to the seeing FWHM of that image and placed both coincident with galaxies and randomly throughout the field.

The fakes were injected into five CCDs randomly selected from two fields; CDFS which is a sparse, high Galactic latitude field and NGC 6101 which is a comparatively crowded, low Galactic latitude field. These fields were chosen to be representative of the range of crowdedness for all fields in this dataset. Fakes were injected for two nights from these two fields, 10 September 2021 and 30 August 2022 for CDFS and 4 August 2016 and 24 June 2019 for NGC 6101. These nights have seeing FWHM values representative of the entire dataset, spanning $1.1''$ to $2''$. A total of 1463 fakes were injected into the images across these four field-nights.

Figure 5 shows the relative difference between injected and recovered flux for both `photpipe` and `dwf-postpipe`. The results from this plot are for fakes injected randomly throughout the field, not those injected onto galaxies. The results are consistent with the limiting magnitude distribution in Figure 2, with a divergence from injected values at $g \sim 22$ AB mag. Fakes with observed peak magnitudes $g < 22$ AB mag are recovered with an efficiency of $97.24^{+0.7}_{-1.0}$ percent for `dwf-postpipe` and $96.14^{+0.9}_{-1.1}$ percent for `photpipe`. There is a sharp drop in recovery efficiency for fakes peaking at $g > 22$ AB mag for both pipelines. However, we find that this drop is shallower for `dwf-postpipe`, resulting in more subthreshold detections. `dwf-postpipe` recovers transients $g > 22$ with an efficiency of $63.9^{+2.7}_{-2.8}$ percent compared to `photpipe`'s $29.3^{+2.7}_{-2.6}$ percent. Given the low signal-to-noise ratio ($<5\sigma$) of these detections, it may be difficult to use them to assess a given transient's nature. In image subtraction, background RMS is increased in quadrature with the template background RMS. Given the depth of our selected templates (23.2 and 23.6 AB mag for NGC 6101 and CDFS respectively), we expect this to result in a difference depth ∼ 0.1 mag shallower than the science images. Therefore, the divergence in recovery efficiency for `dwf-postpipe` and `photpipe` can be likely attributed to the loss of sensitivity imparted by image subtraction. We conclude that

https://doi.org/10.1017/pasa.2025.10140 Published online by Cambridge University Press

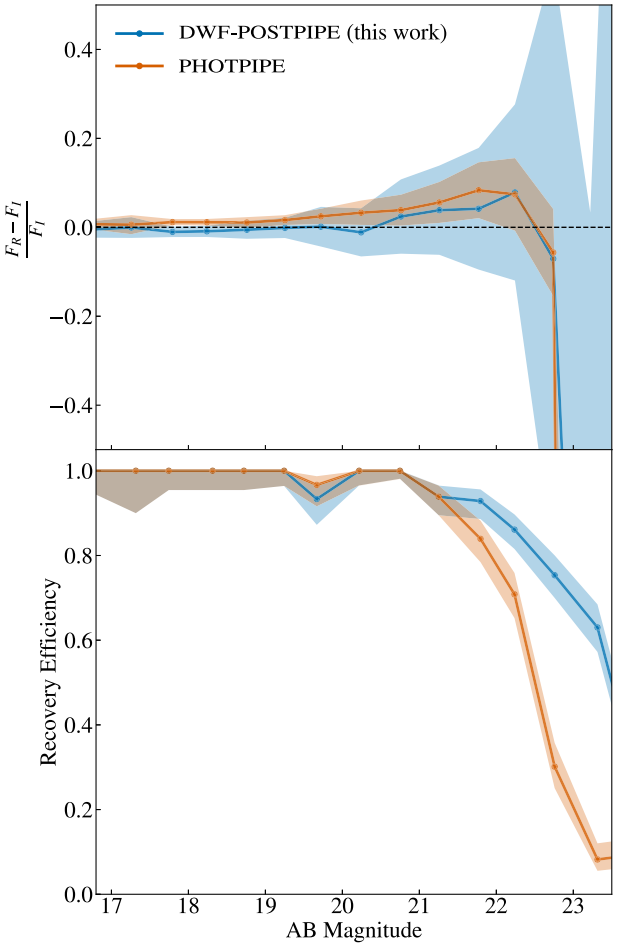


Figure 5. Top panel: Relative difference between the injected flux, F_I and recovered flux, F_R, with injected AB magnitude. These values are calculated from each data point independently from each injected 'fake' source. Bottom panel: Efficiency at which injected fakes with the peak magnitude are recovered as detections using the data processing pipelines `photpipe` and `dwf-postpipe`. Both panels show only the fakes that were injected randomly throughout the field, excluding those that were injected onto galaxies.

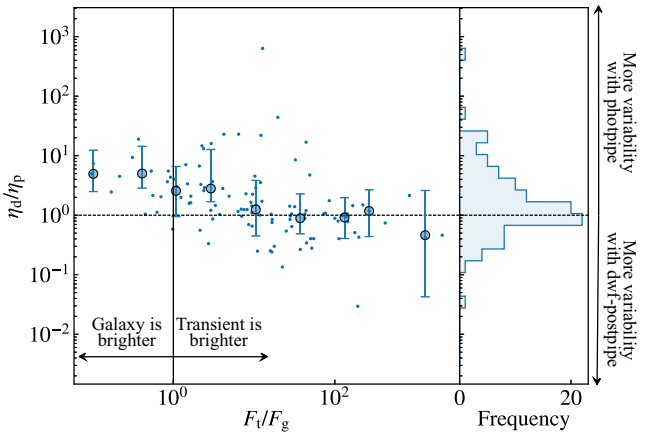


Figure 6. Comparative variability of injected fakes extracted with `dwf-postpipe` compared with `photpipe`. The left-hand panel's *y*-axis is the ratio of the von Neumann statistic from a given light curve extracted with `dwf-postpipe`.η_d to the same light curve extracted with `photpipe`, η_p. Its *x*-axis is the ratio the peak flux density of the injected transient, F_t, to the flux density of the galaxy it has been placed onto, F_g. The small points denote individual injected fakes, while the larger points are the median, binned values with error bars denoting the standard deviations for each bin. For injected fakes where the galaxy light is comparable in brightness to its peak brightness or lower ($F_t/F_g < 10$), variability is more evident in the `photpipe` light curve compared to the `dwf-postpipe` light curve ($\eta_d/\eta_p > 1$). The right-hand panel shows the histogram of η_d/η_p values across the entire plot. We see an excess of high values of η_d/η_p, which are light curves that display more variability when extracted with `photpipe` compared to `dwf-postpipe`.

the two pipelines are roughly equivalent in their source extraction performance.

However, for sources injected into galaxies, noise induced by the galaxy emission reduces the signal-to-noise ratio for `dwf-postpipe` compared to `photpipe`. As `dwf-postpipe` does not employ a difference imaging approach, fast transients are typically identified via the variability evident in their light curves. To quantify variability, we use the von Neumann statistic (von Neumann 1941) which is explained in Section 3.4.

A subset of fakes were injected at the locations of galaxies in the field, identified from `sextractor`'s SPREAD_MODEL parameter, a star/galaxy classifier based on PSF models. Sources with SPREAD_MODEL > 0.01 were assumed to be galaxies. We demonstrate in Figure 6 that, for transients injected into galaxies, the η^{-1} values of light curves extracted with `dwf-postpipe` is lower than those extracted with `photpipe` for the same transient. Therefore, there is less variability evident in these light curves, meaning that, with `dwf-postpipe` these light curves will be less likely than with `photpipe` to be identified as interesting in searches for transient phenomena. Conversely, in the limit where $F_t >> F_g$ the two pipelines measure similar variability for the same transient. This is expected given that, in this regime, the background flux, which is subtracted by `photpipe`, is negligible compared to that of the injected transient.

5. Search for variable phenomena

Whilst DWF's observing strategy is targeted towards the detection of extragalactic fast transients, the depth and cadence of the DECam images, as well as other wavelength data, provide a unique dataset for the detection and characterisation of variable stars, including events ∼2–3 magfainter than current optical catalogues. Typically, surveys like the Dark Energy Survey fold many nights of observations over the course of years to identify variable stars (e.g. Stringer et al. 2021). DWF's high cadence allows for the identification of short period variables (e.g. RR Lyrae, ZZ ceti, contact binaries and delta Scuti variable stars) within a single night's observations. This temporal resolution and 6 consecutive night observing strategy, coupled with the depth afforded by DECam, results in large volumes of the Milky Way being available for the characterisation of these variables.

Beginning in 2025, Rubin's Wide, Fast, Deep survey (WFD) will explore the transient and variable sky at an unprecedented depth and sky coverage. In addition, with WFD's ∼2–5 day cadence, it may take months to properly characterise short period variables. Our identified catalogue of stars, can be cross-matched with Rubin detections. In particular, due to our magnitude limits, we identify faint stars that can improve the target identification for variable star analyses and for reducing contaminants in extragalactic searches with Rubin brokers such as Fink (Möller et al. 2021).

Here, we present searches for variable sources in two fields, NGC Section 5.1 and CDFS, Section 5.2. In particular, The

https://doi.org/10.1017/pasa.2025.10140 Published online by Cambridge University Press

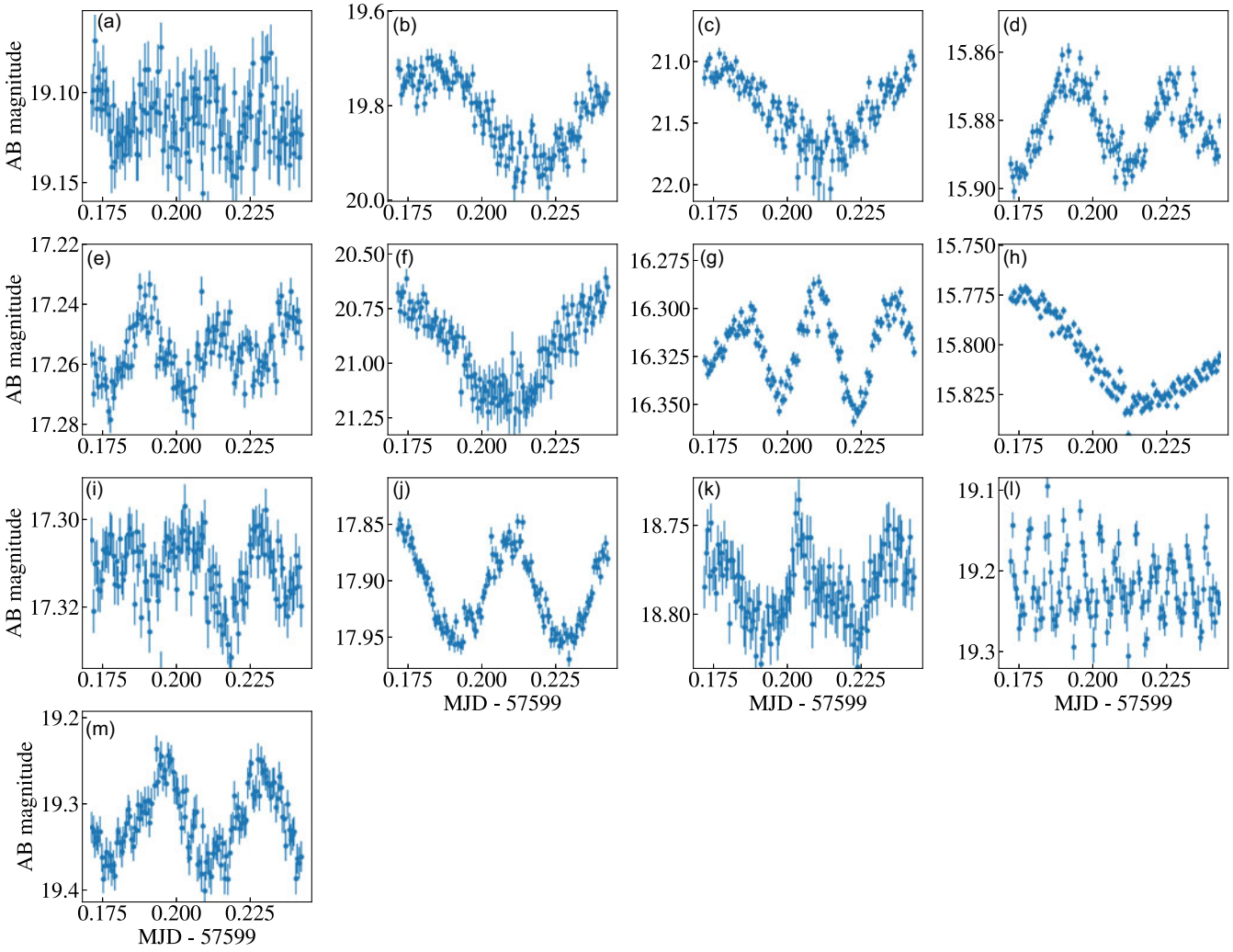


Figure 7. The light curves of uncatalogued periodic sources identified from the DWF data from the field NGC 6101 on the night of 30 July 2016 UTC.

Chandra Deep Field South (CDFS) is a legacy deep field, which was observed as part of DWF field for 9 nights in total (see Table 1). It will also be one of Rubin's deep drilling fields. DWF provides a deep, high cadence survey of CDFS across seven years. These observations could both provide supplementary data to characterise objects of interest identified with Rubin and as a filter to remove contaminants. In Section 5.3, we classify the objects found in this search.

5.1. Periodic sources in NGC 6101

We search a single field-night, NGC 6101 on 30 July 2016 UTC, for uncatalogued, variable stars with periods <2 h. NGC 6101 is the field with the lowest Galactic latitude and would therefore likely yield the highest density of variable stars. We generate a Lomb-Scargle periodogram (Lomb 1976; Scargle 1982; Press & Rybicki 1989) for each source observed over the course of the night with a magnitude error <0.1. We cut sources that are present in variable catalogues *Gaia* DR3 (Gaia Collaboration et al. 2023) and the ASAS-SN catalogue of variable stars (Jayasinghe et al. 2018). Sources are extracted if they have a peak frequency with a significance of $>5\sigma$ above the background. Out of the 33 sources that satisfy this cut, 13 were genuine newly discovered, periodic, astrophysical sources. The light curves of these 13 uncatalogued variable sources are shown in Figure 7 and their properties are summarised in Table 4.

5.2. Variable sources in CDFS

We search for fast-varying objects in the CDFS field observed for nine field-nights during four DWF operational runs. For the purposes of this search, we define a variable object as one that has an intra-night light curve which satisfies $\eta^{-1} > 1$. We restrict this search only to sources that vary on fast, intra-night timescales. We also remove sources that are present in variable star catalogues, including *Gaia* DR3 (Gaia Collaboration et al. 2023), the ASAS-SN catalogue of variable stars (Jayasinghe et al. 2018) and the catalogue for RR Lyrae variable stars in DES Y6 (Stringer et al. 2021). With these cuts, we were left with ∼3 000 objects. After visual inspection of these candidates, all but two of them were assessed to be spurious. The spurious objects were either sources displaying variability due to their proximity to the edge of a CCD, electronic artefacts or their proximity to diffraction spikes from a nearby bright star.

https://doi.org/10.1017/pasa.2025.10140 Published online by Cambridge University Press

Table 4. Properties of the periodic sources found in the DWF observations of NGC 6101. Sources without significant parallax values do not have an associated distance or luminosity measurement.

Candidate	Coordinates	Period (min)	Distance (pc)	m_G (AB mag)	M_G (AB mag)	Suspected class
a)	16:27:02 −72:16:07	27 ± 4	–	19.138 ± 0.004	–	Pulsator
b)	16:16:47 −72:23:05	78 ± 3	$1\,259 \pm 183$	18.203 ± 0.003	7.7 ± 0.3	Eclipsing Binary
c)	16:35:43 −72:33:50	92 ± 7	–	20.79 ± 0.02	–	Pulsator
d)	16:24:45 −72:57:47	51 ± 1	$4\,926 \pm 823$	15.900 ± 0.003	2.4 ± 0.4	Pulsator
e)	16:30:28 −72:51:25	35.1 ± 0.7	–	17.298 ± 0.003	–	Pulsator
f)	16:13:47 −73:05:56	102 ± 19	–	20.23 ± 0.01	–	Eclipsing Binary
g)	16:17:15 −73:05:33	36.3 ± 0.2	$13\,928 \pm 8\,748$	16.429 ± 0.003	0.7 ± 1.4	Pulsator
h)	16:39:27 −73:01:42	92 ± 4	$6\,305 \pm 1\,157$	15.745 ± 0.003	1.7 ± 0.4	Pulsator
i)	16:15:20 −73:15:12	33.9 ± 0.8	$6\,702 \pm 3\,064$	17.320 ± 0.004	3.2 ± 1.0	Pulsator
j)	16:13:09 −73:21:41	54 ± 1	–	17.911 ± 0.003	–	Pulsator
k)	16:30:02 −73:34:47	42 ± 1	$4\,613 \pm 3\,685$	18.834 ± 0.003	5.5 ± 1.7	Pulsator
l)	16:28:36 −73:31:39	8.62 ± 0.03	939 ± 268	19.469 ± 0.004	9.6 ± 0.6	ZZ ceti
m)	16:19:55 −73:45:21	46.2 ± 0.9	–	19.265 ± 0.004	–	Pulsator

Table 5. Summary of variable phenomena found by searching the CDFS field during four DWF operational runs.

Candidate	Coordinates	Peak time UTC	Peak g-band brightness AB magnitude	Quiescent g-band brightness AB magnitude
n)	03:31:40 −29:03:29	2019-12-03T04:26:58	21.39 ± 0.09	22.23 ± 0.03
o)	03:31:34 −27:45:04	2019-12-05T02:56:07	18.52 ± 0.02	22.15 ± 0.03

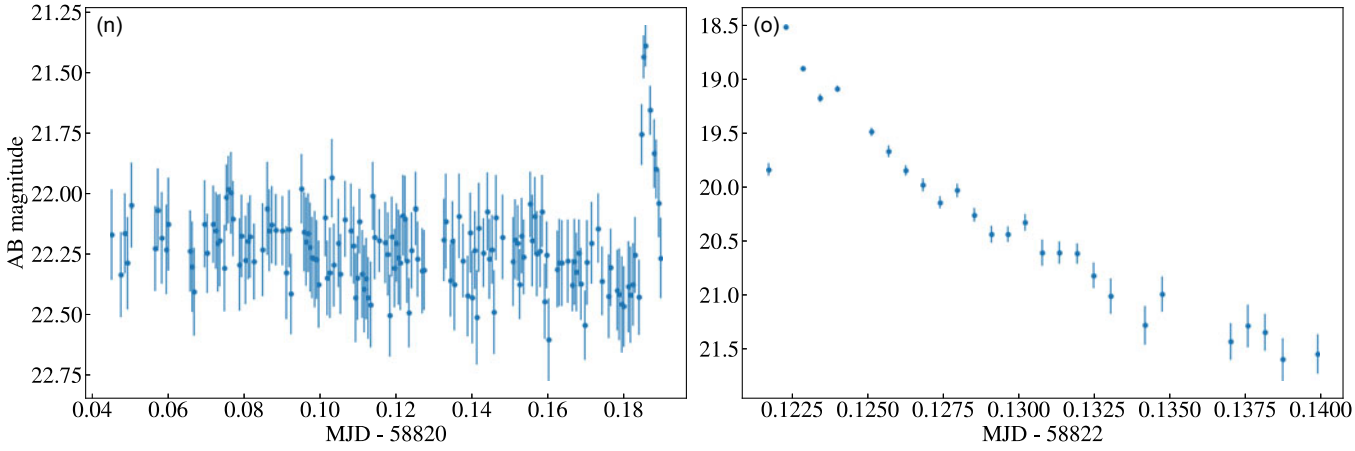


Figure 8. Light curves of variable phenomena (candidates *n* and *o*) found by searching all DWF observations of CDFS.

The remaining two candidates are summarised in Table 5 and their light curves are shown in Figure 8. Neither of these candidates display variability on any nights other than those plotted in Figure 8 and display a fast rise and slower decay which indicates that they are likely eruptive, flare-like events.

5.3. Classification of variable sources

To help classify the periodic sources found in our NGC 6101 field search, we cross-match to Gaia DR3 (Gaia Collaboration et al. 2023) to obtain both parallax and Gaia satellite's Blue and Red Photometer (BP/RP) measurements (De Angeli et al. 2023). This information allows us to construct a colour-magnitude diagram to help determine a spectral classification. The candidates that have coincident detections in Gaia DR3 are presented in Figures 7 and 8. However, whilst all candidates have BP/RP values, a subset either do not have parallax measurements or possess errors larger than the parallax value itself. Despite this, we are able to provide a tentative classification of all sources found in Figure 5. From their location in Figure 9 and the plateau-like phases in their light curves, we classify candidates *b* and *f* as eclipsing binaries. Candidate *l* is likely a ZZ Ceti variable star (e.g. Fontaine & Brassard 2008; Althaus et al. 2010), due to its location in Figure 8 and its short period of 8.62 ± 0.03 min. The remaining candidates

https://doi.org/10.1017/pasa.2025.10140 Published online by Cambridge University Press

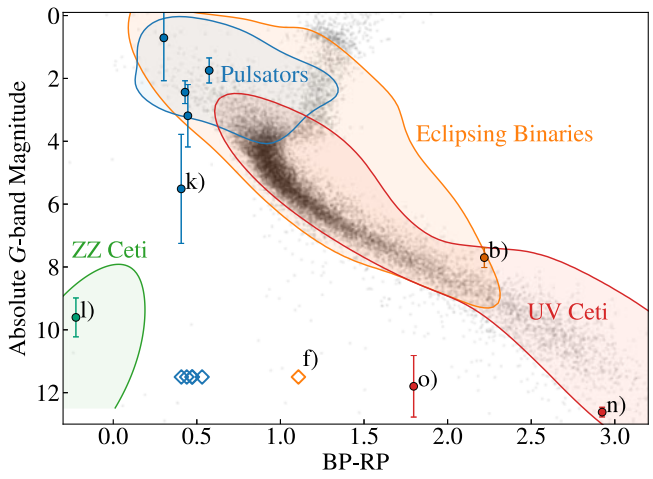


Figure 9. Absolute *G*-band magnitude and BP-RP values of the candidates present in Figures 7 and 8, obtained from Gaia DR3 (Gaia Collaboration et al. 2023). Sources without significant parallax values do not have an associated distance or absolute magnitude measurement and are denoted with diamonds. The black points denote a random sample of Gaia DR3 sources with significant parallax measurements. The contour lines denote the regions in parameter space where different variable star types inhabit. ZZ ceti, eclipsing binaries, UV ceti and pulsating variables are plotted. Pulsating variables include δ Scuti, RR Lyrae and SX Pheonicis type stars. The contours are constructed using sources from The International Variable Star Index Watson et al. (2006), cross-matched with Gaia DR3.

are likely a combination of RR Lyrae, δ Scuti and SX Phoenicis type stars.

For the variable sources found in CDFS, we classify candidate *n* as a UV Ceti due to its location in Figure 9. These are often a low-mass, usually M-class, stars characterised by sporadic flares. However, candidate *o* is subluminous for this population. This could be due to the star being a subdwarf or possessing a blue, faint companion star such as a white dwarf. It also has an X-ray counterpart in the Chandra source catalogue (CXO J033133.7-274505; Evans et al. 2010) and the XMM Newton serendipitous source catalogue (4XMM J033133.7-274505; Webb et al. 2020a).

Given the high galactic latitude ($-54.93°$) and sparsity of CDFS, it is expected that a smaller number of uncatalogued variables would be identified compared to NGC 6101. CDFS is also a well-explored region of sky, meaning it is well populated with public variable star catalogues. From this, we conclude that variable star catalogues will be effective in removing contaminants for well-explored extragalactic fields like CDFS for $g < 22.2$ AB mag.

6. Discussion

6.1. Broader applications and impact

DWF's first optical data release provides a dataset which probes a parameter space poorly characterised by most other transient surveys. We have shown that `dwf-postpipe` provides a set of data products which is effective in extracting science from this dataset, outperforming a difference imaging approach in some scenarios and providing light curves for all sources in the fields. The science-ready data products, available on AAO Data Central, will allow for simple exploration and querying of this vast dataset.

Some of these data have been mined using various methods for extragalactic fast transients (e.g. Andreoni et al. 2020; Freeburn et al. 2024) and stellar flares (e.g. Webb et al. 2020b, 2021), Section 5 and 5.3 has demonstrated that there is potential for studying variable star populations and different transient types and durations via other techniques. The exploration of one night's observations of NGC 6101 here has produced a sample of 13 uncatalogued, fast-evolving, stellar pulsators, with the entire DWF dataset harbouring more. We leave a comprehensive search to future work but this sample would likely provide a number of well understood pulsators such as δ scuti, SX Phoenicus and RR Lyrae type stars. Photometric observations of these stars provide a means of studying stellar interiors via their oscillations (Kjeldsen & Bedding 1995). DWF DR1 probes large Galactic volumes, which may enable population studies of white dwarf pulsators.

While DWF provides limited sky coverage compared to Rubin, DWF DR1 can complement Rubin and its brokers by providing high-cadence coverage sources of interest identified in the Wide, Fast, Deep survey. It will provide characterisation of short period variable stars, sampling their full periods. In addition, in the future, we plan to release the full, multi-wavelength DWF dataset on AAO Data Central including simultaneous radio, high energy and optical data from Subaru/Hyper Suprime-Cam and KMTNeT. We also plan to provide nightly stacked difference imaging, which will reach depths of $g \sim 25$–26 AB mag and will be coupled with multi-band imaging in *r* and *i*-band to constrain colour evolution.

6.2. Future work

In recent years, low read noise, scientific-grade complementary metal-oxide-semiconductor (CMOS) detectors have increasingly been used in astronomical facilities. Their fast readout times result in a cadence unachievable with CCD detectors without sacrificing duty cycle. While CMOS detectors and electron-multiplying CCDs (EMCCDs) on major facilities (e.g. Dhillon et al. 2014; O'Donoghue et al. 2006) have small fields of view, making transient search programs difficult, there are upcoming telescope arrays with wide fields of view. The Large Array Survey Telescope (Ben-Ami et al. 2023) and the upcoming Argus Array (Law et al. 2022) utilise an array of off-the-shelf CMOS detectors to construct observatories with sensitivities equivalent to several meter class telescopes. The Argus Array's instantaneous sky coverage is 7 916 square degrees, reaching a $r \sim 20$ AB mag depth, similar to ZTF, in a few minutes and a $r \sim 22$ AB mag depth, similar to DWF, in one hour. Facilities like these will be the next steps in characterising the dynamic optical sky.

7. Summary

The transient and variable optical sky is poorly characterised at seconds-to-hours timescales. Traditional, current generation, transient surveys such as Zwicky Transient Facility's main survey and the Dark Energy Survey have cadences in excess of a day. Other high cadence surveys such as Evryscope and TESS possess a very wide field-of-view but are comparatively shallow. The Deeper, Wider, Faster programme (DWF), utilising the Dark Energy Camera (DECam), probes a unique parameter space between these two observing strategies, achieving deep ($g \sim 22.2$), minute-cadence observations with a three square degree sky coverage per pointing.

In this work, we present DWF's first data release of optical data products of the minute-cadence DECam observations collected during the 14 DWF observing runs to-date (excludes Subaru Hyper Suprime-Cam and KMTNet observations). The dataset includes 112 DECam pointings, each with 0.5–3 h of continuous,

https://doi.org/10.1017/pasa.2025.10140 Published online by Cambridge University Press

minute-cadence, observations and a cumulative time on-sky time of 166 h.

The data products were produced from a novel data processing pipeline, `dwf-postpipe`. For each field, for each night, this pipeline takes in calibrated images from the DECam community pipeline and outputs lightcurves for every source in the field. It does this in three steps; identifying all transient and quiescent sources visible throughout each night's images, aligning these images to a 'detection image' and finally using this detection image to extract time-resolved photometry. The result is a rich set of observations of transient and variable phenomena that are publicly available on AAO Data Central.

These observations reach a median 5σ depth of 22.2 AB mag and a median seeing FWHM of 1.35″. We assess the data quality by comparing our photometric measurements of quiescent sources to that of DELVE. We found our observations, calibrated with *SkyMapper* DR4, have a consistent, systematic, ∼0.15 mag offset from DELVE. Fake sources were injected directly into images, extracted, and light curves generated to compare the efficiency and recovery of transients with a typical difference imaging approach for DECam, `photpipe`. We find similar performance with the two approaches to 22 AB mag and an efficiency of $97.24^{+0.7}_{-1.0}$ percent for `dwf-postpipe` and $96.14^{+0.9}_{-1.1}$ percent for `photpipe`. `dwf-postpipe` recovers a greater number of subthreshold transients $g > 22$ with an efficiency of $63.9^{+2.7}_{-2.8}$ percent compared to `photpipe`'s $29.3^{+2.7}_{-2.6}$ percent. We attribute this to the loss of sensitivity imparted by image subtraction. However, we note that as `dwf-postpipe` measures photometry directly on the science images, transients with a comparatively bright background galaxy are difficult to identify as the variability in the transient signal competes with the noise induced by the underlying host galaxy emission.

Whilst DWF is a unique survey for identifying fast transients, it also provides a unique avenue to study variable stars. In a search for uncatalogued variable stars in one night of DWF observations of one field, NGC 6101, we find 13 such sources. Of these sources ten are pulsating variables, two are eclipsing binaries and one is a ZZ ceti star.

DWF's observations of Chandra Deep Field South, a Rubin deep-drilling field, provides a dataset to flag rapidly evolving and faint variable sources which may take many months/years before they are identified and characterised as a result of Rubin's observational cadence. We search nine nights of DWF observations of CDFS for uncatalogued faint variable sources and identify two flares from likely UV ceti type stars. From this, we conclude that in CDFS and, more generally, deep, extragalactic, legacy fields existing optical variable star catalogues are effective in removing variable star contaminants to $g < 22.2$ AB mag. In the Rubin-era, these catalogues will play a crucial role in filtering in the deep-drilling fields which will allow for more efficient detection of novel, extragalactic transients (e.g. Freeburn et al. 2025b).

Acknowledgements. We thank Courtney Crawford and Ben Montet for valuable discussions regarding variable star candidate identification and classification.

We also thank the anonymous referee for their insightful comments.

J.C. acknowledges funding by the Australian Research Council Discovery Project, DP200102102.

A.M. is supported by the Australian Research Council DE230100055.

Parts of this research were conducted by the Australian Research Council Centre of Excellence for Gravitational Wave Discovery (OzGrav), through project numbers CE170100004 and CE230100016.

This paper includes data that has been provided by the AAO Data Central Science Platform (datacentral.org.au) and makes use of services and code that have been provided by the AAO Data Central Science Platform.

This project used data obtained with the Dark Energy Camera (DECam), which was constructed by the Dark Energy Survey (DES) collaboration. Funding for the DES Projects has been provided by the US Department of Energy, the U.S. National Science Foundation, the Ministry of Science and Education of Spain, the Science and Technology Facilities Council of the United Kingdom, the Higher Education Funding Council for England, the National Center for Supercomputing Applications at the University of Illinois at Urbana-Champaign, the Kavli Institute for Cosmological Physics at the University of Chicago, Center for Cosmology and Astro-Particle Physics at the Ohio State University, the Mitchell Institute for Fundamental Physics and Astronomy at Texas A&M University, Financiadora de Estudos e Projetos, Fundação Carlos Chagas Filho de Amparo à Pesquisa do Estado do Rio de Janeiro, Conselho Nacional de Desenvolvimento Cientfico e Tecnológico and the Ministério da Ciência, Tecnologia e Inovação, the Deutsche Forschungsgemeinschaft and the Collaborating Institutions in the Dark Energy Survey.

The Collaborating Institutions are Argonne National Laboratory, the University of California at Santa Cruz, the University of Cambridge, Centro de Investigaciones Enérgeticas, Medioambientales y Tecnológicas–Madrid, the University of Chicago, University College London, the DES-Brazil Consortium, the University of Edinburgh, the Eidgenössische Technische Hochschule (ETH) Zürich, Fermi National Accelerator Laboratory, the University of Illinois at Urbana-Champaign, the Institut de Ciències de l'Espai (IEEC/CSIC), the Institut de Fsica d'Altes Energies, Lawrence Berkeley National Laboratory, the Ludwig-Maximilians Universität München and the associated Excellence Cluster Universe, the University of Michigan, NSF NOIRLab, the University of Nottingham, the Ohio State University, the OzDES Membership Consortium, the University of Pennsylvania, the University of Portsmouth, SLAC National Accelerator Laboratory, Stanford University, the University of Sussex, and Texas A&M University.

Based on observations at NSF Cerro Tololo Inter-American Observatory, NSF NOIRLab (NOIRLab Prop. ID 2020B-0253; PI: J. Cooke), which is managed by the Association of Universities for Research in Astronomy (AURA) under a cooperative agreement with the U.S. National Science Foundation.

This research made use of `matplotlib`, a Python library for publication quality graphics (Hunter 2007), `SciPy` (Virtanen et al. 2020), `Astropy`, a community-developed core Python package for Astronomy (Astropy Collaboration et al. 2013; Astropy Collaboration et al. 2018) and `scikit-learn` (Pedregosa et al. 2011).

Data availability statement. The photometry and image cutouts can be queried on AAO Data Central (https://doi.org/10.57891/gy62-bj96) and includes a range of summary statistics and catalogue cross-matches. Raw and calibrated images are available on the NOIRLab Astro Data Archive under program numbers 2015B-0607, 2016A-0095, 2017A-0909, 2019A-0911, 2018A-0137, 2019B-1012 and 2020B-0253. Observations that are still within the 18-month proprietary period and all other code and data underlying this work will be shared upon reasonable request to the authors.

References

Akerlof, C., et al. 1999, Natur, 398, 400
Althaus, L. G., Córsico, A. H., Isern, J., & Garca-Berro, E. 2010, A&ARv, 18, 471
Andreoni, I., & Cooke, J. 2019, in IAU Symposium, Vol. 339, Southern Horizons in Time-Domain Astronomy, ed. R. E. Griffin, 135
Andreoni, I., et al. 2017, PASA, 34, e037
Andreoni, I., et al. 2020, MNRAS, 491, 5852
Andreoni, I., et al. 2022, Natur, 612, 430
Astropy Collaboration, et al. 2013, A&A, 558, A33
Astropy Collaboration, et al. 2018, AJ, 156, 123

Becker, A. 2015, HOTPANTS: High Order Transform of PSF ANd Template Subtraction, Astrophysics Source Code Library, record ascl:1504.004, ascl:1504.004
Bellm, E. C., et al. 2019, PASP, 131, 018002
Ben-Ami, S., et al. 2023, PASP, 135, 085002
Berger, E., et al. 2013, ApJ, 779, 18
Bersten, M. C., et al. 2018, Natur, 554, 497
Bertin, E. 2010, SWarp: Resampling and Co-adding FITS Images Together, Astrophysics Source Code Library, record ascl:1010.068, ascl:1010.068
Bertin, E., & Arnouts, S. 1996, SExtractor: Software for source extraction. doi: 10.1051/aas:1996164
Clarke, R., et al. 2025, arXiv e-prints, arXiv:2507.19584
Dark Energy Survey Collaboration, et al. 2016, MNRAS, 460, 1270
De Angeli, F., et al. 2023, A&A, 674, A2
Dhillon, V. S., et al. 2014, MNRAS, 444, 4009
Dobie, D., et al. 2023, MNRAS, 519, 4684
Drlica-Wagner, A., et al. 2021, ApJS, 256, 2
Evans, I. N., et al. 2010, ApJS, 189, 37
Falcke, H., & Rezzolla, L. 2014, A&A, 562, A137
Flaugher, B., et al. 2015, AJ, 150, 150
Fontaine, G., & Brassard, P. 2008, PASP, 120, 1043
Freeburn, J., et al. 2024, MNRAS, 531, 4836
Freeburn, J., et al. 2025a, MNRAS, 537, 2061
Freeburn, J., et al. 2025b, arXiv e-prints, arXiv:2507.22864
Gaia Collaboration, et al. 2023, A&A, 674, A1
Galama, T., et al. 1997, Natur, 387, 479
Garnavich, P. M., et al. 2016, ApJ, 820, 23
Goode, S., et al. 2022, MNRAS, 513, 1742
Haisch, B., Strong, K. T., & Rodono, M. 1991, ARA&A, 29, 275
Hanmer, K. Y., et al. 2025, MNRAS, 538, 1800
Hjorth, J., et al. 2005, Natur, 437, 859
Ho, A., et al. 2024, Transient Name Server AstroNote, 135, 1
Ho, A. Y. Q., et al. 2022, ApJ, 938, 85
Ho, A. Y. Q., et al. 2023, Natur, 623, 927
Howard, W. S., et al. 2019, ApJ, 881, 9
Howard, W. S., et al. 2018, ApJ, 860, L30
Hunter, J. D. 2007, CSE, 9, 90
Ivezić, Ž., et al. 2019, ApJ, 873, 111
Jayaraman, R., Fausnaugh, M., Ricker, G. R., Vanderspek, R., & Mo, G. 2024, ApJ, 972, 162
Jayasinghe, T., et al. 2018, MNRAS, 477, 3145
Kaiser, N., et al. 2002, in Society of Photo-Optical Instrumentation Engineers (SPIE) Conference Series, Vol. 4836, Survey and Other Telescope Technologies and Discoveries, ed. J. A. Tyson, & S. Wolff, 154
Kim, S.-L., et al. 2016, JKoAS, 49, 37
Kjeldsen, H., & Bedding, T. R. 1995, A&A, 293, 87
Klebesadel, R. W., Strong, I. B., & Olson, R. A. 1973, ApJ, 182, L85
Klein, C., Bellm, E., & Davenport, J. 2019, in American Astronomical Society Meeting Abstracts, Vol. 233, American Astronomical Society Meeting Abstracts #233, 259.21
Kupfer, T., et al. 2021, MNRAS, 505, 1254
Lamb, G. P., & Kobayashi, S. 2019, MNRAS, 489, 1820
Law, N. M., et al. 2015, PASP, 127, 234
Law, N. M., et al. 2022, PASP, 134, 035003
Levan, A. J., et al. 2024, Nature, 626, 737
Lomb, N. R. 1976, Ap&SS, 39, 447
Long, K., & Pe'er, A. 2018, ApJ, 864, L12
Lorimer, D. R., Bailes, M., McLaughlin, M. A., Narkevic, D. J., & Crawford, F. 2007, Sci, 318, 777
Margalit, B., Berger, E., & Metzger, B. D. 2019, ApJ, 886, 110
Meade, B., et al. 2017, PASA, 34, e023
Metzger, B. D., Margalit, B., & Sironi, L. 2019, MNRAS, 485, 4091
Miyazaki, S., et al. 2002, PASJ, 54, 833
Moffett, T. J. 1974, ApJS, 29, 1
Möller, A., et al. 2021, MNRAS, 501, 3272
Nakar, E., & Sari, R. 2010, ApJ, 725, 904
Núñez, C., et al. 2021, A&A, 653, A119
O'Donoghue, D., et al. 2006, MNRAS, 372, 151
Oganesyan, G., et al. 2023, NatAs, 7, 843
Onken, C. A., et al. 2024, PASA, 41, e061
Pedregosa, F., et al. 2011, JMLR, 12, 2825
Perley, D. A., et al. 2020, ApJ, 904, 35
Perley, D. A., et al. 2025, MNRAS, 537, 2362
Press, W. H., & Rybicki, G. B. 1989, ApJ, 338, 277
Price, D. C., et al. 2018, RNAAS, 2, 30
Quirola-Vásquez, J., et al. 2022, A&A, 663, A168
Quirola-Vásquez, J., et al. 2023, A&A, 675, A44
Rest, A., et al. 2005, ApJ, 634, 1103
Rest, A., et al. 2014, ApJ, 795, 44
Ricker, G. R., et al. 2015, JATIS, 1, 014003
Roxburgh, H., et al. 2024, ApJ, 963, 89
Roxburgh, H., et al. 2025, arXiv e-prints, arXiv:2502.16905
Ryan, G., van Eerten, H., Piro, L., & Troja, E. 2020, ApJ, 896, 166
Scargle, J. D. 1982, ApJ, 263, 835
Schawinski, K., et al. 2008, Sci, 321, 223
Sokolovsky, K. V., et al. 2017, MNRAS, 464, 274
Strausbaugh, R., et al. 2022, AJ, 163, 95
Stringer, K. M., et al. 2021, ApJ, 911, 109
Taylor, M. B. 2005, in Astronomical Society of the Pacific Conference Series, Vol. 347, Astronomical Data Analysis Software and Systems XIV, ed. P. Shopbell, M. Britton, & R. Ebert, 29
Tingay, S. J., & Yang, Y.-P. 2019, ApJ, 881, 30
Tonry, J. L., et al. 2018, ApJ, 867, 105
Valdes, F., Gruendl, R., & DES Project. 2014, in Astronomical Society of the Pacific Conference Series, Vol. 485, Astronomical Data Analysis Software and Systems XXIII, ed. N. Manset, & P. Forshay, 379
Van Bemmel, N., et al. 2025, MNRAS, 537, 3332
Villasenor, J. S., et al. 2005, Natur, 437, 855
Virtanen, P., et al. 2020, NM, 17, 261
von Neumann, J. 1941, AnMS, 12, 367
Watson, C. L., Henden, A. A., & Price, A. 2006, Society for Astronomical Sciences Annual Symposium, 25, 47
Webb, N. A., et al. 2020a, A&A, 641, A136
Webb, S., et al. 2020b, MNRAS, 498, 3077
Webb, S., et al. 2021, MNRAS, 506, 2089
Yang, Y.-P., Zhang, B., & Wei, J.-Y. 2019, ApJ, 878, 89
Yi, S.-X., Gao, H., & Zhang, B. 2014, ApJ, 792, L21

Appendix A. Error correction calculation

Performing a Gaussian convolution on an image with a FWHM of σ_c, neighbouring pixels become correlated. This reduces the effective number of independent pixels, N_A, compared to the actual number of pixels in the convolved image, N, summed to calculate the flux, f

$$N_A = \frac{N}{2\pi\sigma_c} \tag{A1}$$

The background variance, σ^2_{bkg}, is calculated globally from all pixels in the image, and is conserved when the image is convolved

$$\sigma^2_{\mathrm{bkg/pix}} = \sigma^2_{\mathrm{bkg/pix},c} \tag{A2}$$

$$\sigma^2_{\mathrm{bkg}} = N_A\sigma^2_{\mathrm{bkg/pix},c} = \frac{1}{2\pi\sigma_c}\sigma^2_{\mathrm{bkg},c} \tag{A3}$$

The root-mean-squared error for a given source, σ^2_{src} is given by the sum of the variance due the shot noise, σ^2_{shot} and background noise, σ^2_{bkg}

$$\sigma^2_{\mathrm{src}} = \sigma^2_{\mathrm{shot}} + \sigma^2_{\mathrm{bkg}} \tag{A4}$$

$$= \frac{1}{g}\sum_i^{N_A} f_i + \sigma^2_{\mathrm{bkg}} \tag{A5}$$

https://doi.org/10.1017/pasa.2025.10140 Published online by Cambridge University Press

where g is the gain. Assuming the flux for a given source in the convolved image is conserved,

$$\sigma^2_{\rm src} = \frac{1}{2\pi\sigma_c}\frac{1}{g}\sum_i^N f_{i,c} + \sigma^2_{\rm bkg} \tag{A6}$$

$$= 2\pi\sigma_c\left(\sigma^2_{{\rm shot},c} + \sigma^2_{{\rm src},c}\right) \tag{A7}$$

$$= \alpha\left(\sigma^2_{{\rm shot},c} + \sigma^2_{{\rm src},c}\right) \tag{A8}$$

Assuming two consecutive images have similar seeing and depth, we can calculate α by comparing the median difference in flux $\bar{f}_{{\rm diff},j}$ between consecutive images to the median flux error $\bar{\sigma}_{{\rm src},c,j}$, for infinitesimal flux bins which have a median flux, $\bar{f}_j$. Using Equation (A8),

$$\alpha = \frac{\bar{f}^2_{{\rm diff},j}}{\bar{f}^2_j} \tag{A9}$$

Appendix B. Catalogue schema

Table B1. Columns in the `mastercatalogue` catalogue.

Name	Description	Unit
`candidate_id`	Unique identifier for each transient or variable candidate	–
`ccd`	Charge-coupled device identifier on the Dark Energy Camera	–
`night`	Observing night identifier (YYYYMMDD format)	–
`ra`	Right Ascension of the candidate	deg
`dec`	Declination of the candidate	deg
`mjd_start`	Modified Julian Date at the start of observations	days
`mjd_end`	Modified Julian Date at the end of observations	days
`mjd_mid`	Modified Julian Date at the midpoint of observations	days
`med_uplim`	Median upper limit magnitude of observations	AB mag
`var`	von Neumann statistic of light curve	–
`detections`	Number of detections of the source	–
`max_mag`	Faintest observed *g*-band magnitude (highest numerical value)	AB mag
`min_mag`	Brightest observed *g*-band magnitude (lowest numerical value)	AB mag
`stdmag`	Standard deviation of the observed magnitudes	AB mag
`mederr`	Median photometric uncertainty of the detections	AB mag
`medmag`	Median observed *g*-band magnitude	AB mag

Table B2. Columns in the `lightcurve` catalogue.

Name	Description	Unit
`candidate_id`	Unique identifier for each transient or variable candidate	–
`ccd`	Charge-coupled device identifier on the Dark Energy Camera	–
`night`	Observing night identifier (YYYYMMDD format)	–
`mjd`	Modified Julian Date of the observation	days
`x_pix`	*X* coordinate of the source centroid in image pixels	pixel
`y_pix`	*Y* coordinate of the source centroid in image pixels	pixel
`ra`	Right Ascension of the source	deg
`dec`	Declination of the source	deg
`flux`	Measured source flux in *g*-band	μJy
`flux_err`	Uncertainty in measured flux	μJy
`mag`	Measured *g*-band magnitude	AB mag
`mag_err`	Uncertainty in measured magnitude	AB mag
`fwhm_pix`	Full Width at Half Maximum of the source in image pixels	pixel
`fwhm`	Full Width at Half Maximum of the source in arcseconds	″
`ellipticity`	Ellipticity of the source profile ($1 - B/A$)	–
`limiting_mag`	Limiting magnitude (5-sigma) for the observation	AB mag
`filename`	Name of the image file containing the measurement	–

https://doi.org/10.1017/pasa.2025.10140 Published online by Cambridge University Press